Impact of boundary conditions on the modeled thermal regime of the Antarctic ice sheet

In-Woo Park[1], Emilia Kyung Jin[2], Mathieu Morlighem[3], and Kang-Kun Lee[1]

[1]School of Earth and Environmental Sciences Seoul National University, Seoul, South Korea
[2]Korea Polar Research Institute, Incheon, South Korea
[3]Department of Earth Sciences, Dartmouth College, Hanover NH, USA

Correspondence: jin@kopri.re.kr

Abstract. A realistic initialization of ice flow models is critical for predicting future changes in ice sheet mass balance and their associated contribution to sea level rise. The initial thermal state of an ice sheet is particularly important as it controls ice viscosity and basal conditions, thereby influencing the overall ice velocity. Englacial and subglacial conditions, however, remain poorly understood due to insufficient direct measurements, which complicates the initialization and validation of thermal models. Here, we investigate the impact of using different geothermal heat flux (GHF) datasets and vertical velocity profiles on the thermal state of the Antarctic ice sheet, and compare our modeled temperatures to in situ measurements from 15 boreholes. We find that the vertical velocity plays a more important role in the temperature profile than GHF. More importantly, we find that the standard approach, which consists in combining basal sliding speed and incompressibility to derive vertical velocities, provides reasonably good results in fast flowing regions (ice velocity > 50 m yr^{-1}), but performs poorly in slower moving regions.

1 Introduction

Global warming has been responsible for rapid sea level rise from the mass loss of ice sheets and glaciers over the past few decades. The mass loss of the Antarctic ice sheet has more than tripled over the past three decades (IPCC AR6 Chapter 9; Fox-Kemper et al., 2021). The retrograde bed slopes in deep submarine basins (Schoof, 2007), the intrusion of warm water in ice shelf cavities (Alley et al., 2016), and the collapse of ice shelves can accelerate this mass loss (Scambos, 2004), especially in West Antarctica. Ice sheet models have been developed to capture these processes (e.g., Larour et al., 2012b; Gillet-Chaulet et al., 2012; Pollard and DeConto, 2012) and provide projections of future contributions of the ice sheets to sea level rise under different warming scenarios (DeConto and Pollard, 2016; Seroussi et al., 2020). However, the uncertainty in these projections remains high partly due to poorly constrained model inputs, such as bed geometry, basal conditions, ice mechanical properties, or oversimplified parameterization of melting rates under floating ice shelves (e.g., Schlegel et al., 2013; Brondex et al., 2019).

A critical aspect of ice sheet models is their initial conditions. Several important properties, such as ice elevation, surface ice velocities, can be directly observed at the surface of the ice sheet, whereas observing englacial and subglacial properties, such as ice temperature, geothermal heat flux, remain particularly challenging, and direct measurements of these properties are scarce.

25   In order to get a reasonable estimate of these quantities, such as basal friction or ice shelf rigidity, are routinely estimated through inversion techniques (MacAyeal, 1993; Khazendar et al., 2007; Morlighem et al., 2010; Gillet-Chaulet, 2020). These inverse modeling approaches have not been applied to the ice thermal regime of the ice sheet, which remains highly uncertain despite its critical control on ice viscosity and basal friction. Critically, the Geothermal Heat Flux (GHF) is an important parameter that affects basal temperature, water production, and ice dynamics (Pattyn et al., 2008; Seroussi et al., 2017; Smith-
30 Johnsen et al., 2020b) but large uncertainties in spatial variation and magnitude of GHFs in Antarctica still remain.

Previous studies have attempted to infer the GHFs using different methods such as a seismic model (Shapiro and Ritzwoller, 2004; An et al., 2015), magnetic satellite data (Maule et al., 2005), and a combination of seismic and magnetic satellite data (Martos et al., 2017). The most accurate measurements are from in situ borehole measurements of temperature profiles that can be used to constrain the GHFs (Dahl-Jensen et al., 1999; Mony et al., 2020; Talalay et al., 2020).

35   While drilling boreholes requires a lot of resources and efforts, the boreholes provide critical insights into subsurface conditions and lead to a better understanding of the current sub and englacial environments as well as past climate (Augustin and Antonelli, 2002; Motoyama, 2007; Slawny et al., 2014; Fisher et al., 2015; Priscu et al., 2021; Mulvaney et al., 2021; Smith et al., 2021). Borehole temperature profiles can also be utilized to validate thermo-mechanical ice sheet models. As boreholes provide vertical temperature profiles, a one-dimensional thermal model is generally utilized to estimate GHFs (Mony et al.,
40 2020) and reconstruct past climates (Zagorodnov et al., 2012; Yang et al., 2018). Since one-dimensional thermal models typically neglect horizontal advection and only consider vertical advection and diffusion (Engelhardt, 2004a; Mony et al., 2020; Talalay et al., 2020), one-dimensional thermal models have strong limitations and may not be applicable in regions of fast flow. The vertical velocities used in one-dimensional thermal model are generally recovered through the equation of incompressbility, assuming a stationary bed and no sliding (Hindmarsh, 1999). Only a handful of three-dimensional thermo-mechanical ice
45 sheet models have utilized these borehole temperature profiles for validation (Joughin et al., 2004; Pattyn, 2010; Seroussi et al., 2013). Moreover, measurements of borehole temperatures in fast flowing sectors remain scarce due to technical difficulty of drilling boreholes in these regions (Engelhardt, 2004b; Doyle et al., 2018; Anker et al., 2021).

In addition to being sensitive to the GHF, the ice thermal regime is also particularly sensitive to horizontal and vertical ice velocities. While surface ice velocities can be spatially and temporally observed through satellite remote sensing (Mouginot
50 et al., 2012; Derkacheva et al., 2020), englacial velocities are difficult to observe remotely. Few measurements of internal vertical ice velocities are available through direct methods, such as optic-fiber instruments (Pettit et al., 2011), and borehole optical televiewer (OPTV) logging (Hubbard et al., 2020), or indirect methods, such as phase-sensitive radio echo sounder (Gillet-Chaulet et al., 2011; Kingslake et al., 2014). Due to scarcities of internal ice velocity measurements, three-dimensional mechanical models, such as Higher-Order (HO) and Full Stokes (FS), are used to estimate internal ice velocities (Pattyn,
55 2003; Larour et al., 2012b). The ice velocities from mechanical models can, in turn, be used as input variables to compute three-dimensional ice temperature.

Overall, the difficulty in estimating GHF combined with the lack of observations of subsurface ice velocities and temperature limits our ability to capture the thermal regime of the ice sheet and increases the uncertainty in future mass projections. Here, we perform a suite of sensitivity experiments using a three-dimensional thermo-mechanical model using various GHF sources and

60 different approaches to construct vertical ice velocities. We then compare each modeled temperature to 15 temperature profiles from in situ borehole drilling campaigns, including 3 boreholes located in fast flow regions to determine which combination of parameters best reproduces measured temperature profiles.

2 Methods

2.1 Ice flow model

65 We used the Ice-sheet and Sea-level System Model (ISSM) to model the stress balance and thermal state across the entire Antarctic continent (Larour et al., 2012b). We relied on an anisotropic mesh with a resolution varying from 2 km in coastal regions to 40 km near ice divides, and refined the mesh to 2 km mesh around the locations of boreholes where temperature measurements were available. The mesh comprised a total of over a million prismatic elements distributed vertically over 15 layers. We used a 3D HO model and assumed that the ice viscosity follows Glen's flow (Glen, 1955):

$$70 \quad \mu = \frac{B}{2 \, \dot{\varepsilon}_e^{\frac{n-1}{n}}} \tag{1}$$

where B is the ice rigidity (Pa s$^{-1/3}$), $\dot{\varepsilon}_e$ is the effective strain rate (s^{-1}), and n is Glen's law exponent, whose value was 3 in this study. We also utilized the Budd type friction law (Budd et al., 1979; Morlighem et al., 2010):

$$\boldsymbol{\tau}_b = -\alpha^2 N \, \boldsymbol{v}_b \tag{2}$$

where α is the friction coefficient (yr$^{0.5}$ m$^{-0.5}$), N is the effective pressure (taken here as simply $\rho_i g H + \rho_w g \max(0, b)$),
75 and $\boldsymbol{v}_b$ is the basal ice velocity vector. ρ_i is the ice density, ρ_w is the water density, H is the ice thickness, and b is the bed elevation with respect to sea level. The friction coefficient under grounded ice and the ice rigidity of floating ice shelves were estimated based on an inverse method (Morlighem et al., 2010), and the ice rigidity under grounded ice was estimated using the temperature-rigidity relation (Cuffey and Paterson, 2010).

We used an enthalpy model that considers the transition between cold and temperate ice as well as the conservation of the
80 total energy balance (Aschwanden et al., 2012; Seroussi et al., 2013; Kleiner et al., 2015). Here, the enthalpy model is referred to as the thermal model and assumed that the ice is in thermal steady-state:

$$0 = -\boldsymbol{v} \cdot \nabla E + \phi_i + \begin{cases} \nabla \cdot \left(\dfrac{k_i}{c_i \rho_i} \nabla E \right), & \text{if } E < E_s \\[2ex] \nabla \cdot (k \nabla T_{pmp} + k_0 \nabla E), & \text{if } E \geq E_s \end{cases} \tag{3}$$

where $\boldsymbol{v} = (v_x, v_y, v_z)$ is the ice velocity vector, E is the enthalpy, ϕ_i is the internal deformation heat, E_s is the enthalpy of pure ice, $k = (1 - \omega)k_i + \omega k_w$ is the mixture thermal conductivity (with ω representing water content), k_i and k_w are the

85 thermal conductivity of pure ice and liquid water, k_0 is a small positive constant (Aschwanden et al., 2012), c_i is the heat capacity of ice, and T_{pmp} is the pressure melting point of ice.

The surface temperature was constrained using mean 2-m air temperature data from ERA-Interim, which assimilated the recent atmospheric conditions from 1979 to 2018 with a $0.125° \times 0.125°$ resolution (Dee et al., 2011). At the bottom, we imposed a Neumann boundary condition with a heat flux from GHF and frictional heating. The basal temperature under

90 floating ice shelves was set to the pressure melting point. An anisotropic Streamline Upwind Petrov–Galerkin (SUPG) method was adopted since it is more accurate than the original SUPG scheme, which is sensitive to low aspect ratios between the horizontal and vertical resolution meshes (Rückamp et al., 2020). The stress balance and thermal state are closely coupled because the internal deformation and frictional heat from the stress balance affect the thermal model. In turn, the ice rigidity inferred from the thermal model influences the stress balance model. To capture this coupling and reach thermo-mechanical

95 consistency, we iterated 10 times by solving iteratively the stress balance and thermal model until we reach convergence. The convergence was reached when the difference in mean basal temperature was lower than $0.5°C$ between two consecutive iterations.

We used the surface elevation from the Reference Elevation Model of Antarctica (REMA, Howat et al., 2019). The bed geometry is from BedMachine (Morlighem et al., 2020), which used the mass conservation method to generate the bed geometry

100 in fast flow regions and streamline diffusion slow moving regions (Morlighem et al., 2010).

2.2   Vertical velocities

We computed the thermal state of the ice sheet using three different vertical velocity profiles: 1) vertical velocity computed by solving for incompressibility while accounting for the inferred basal sliding (hereafter IVz), and 2) the equation of incompressibility of ice while not allowing basal sliding when surface ice velocities are below 10 m yr^{-1} (hereafter IVz-nosliding).

105 In other words, IVz ignores the inferred basal sliding velocities from the initial inversion and assumes that the bed is frozen when surface velocities are $< 10 \text{ m yr}^{-1}$.

For IVz and IVz-nosliding, we recovered the vertical velocity from the continuity equation as follows:

$$v_z\left(z\right) = v_z\left(b\right) + \int\limits_{b}^{z} -\frac{\partial v_x}{\partial x} - \frac{\partial v_y}{\partial y}\, dz' \tag{4}$$

For IVz-nosliding, we set $v_z\left(b\right) = 0$, while for IVz, the basal vertical velocity was set as:

110 $$v_z\left(b\right) = v_x\left(b\right)\frac{\partial b}{\partial x} + v_y\left(b\right)\frac{\partial b}{\partial y} - \dot{M_b} \tag{5}$$

where $\dot{M_b}$ is the basal melting rate (in m yr^{-1} ice equivalent).

2.3   Geothermal heat flux

We compared four different geothermal flux datasets: Shapiro and Ritzwoller (2004) (SR), which used a seismic model to exptrapolate heat-flow measurements, 2) Maule et al. (2005) (Maule), which used a magnetic model with satellite magnetic
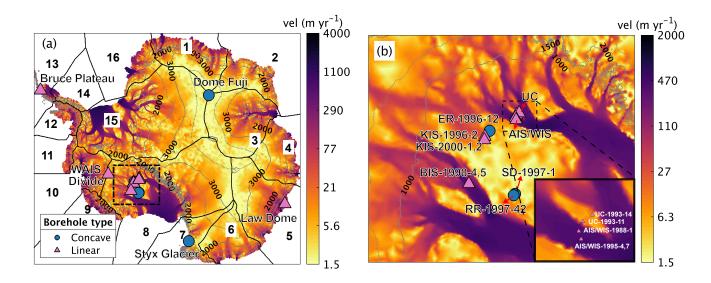
Figure 1. (a) Borehole locations with temperature measurements overlaid over ice velocity (Mouginot et al., 2012). The black dashed box shows the location of (b). The black solid box in (a) indicates each basin from Jourdain et al. (2020), and each number indicates each basin number. We use different symbols for each borehole based on the shape of their temperature profile (triangle and cross red dots indicate concave and linear profiles, respectively). The grey contours indicate surface elevations, with dash lines for every 500 m and solid lines for every 1000 m. (b) Enlargement of borehole locations at West Antarctica overlain over the ice velocity. The borehole names are abbreviated: WIS, Whillans Ice Stream; BIS, Bindschadler Ice Stream; ER, Engelhardt Ridge; KIS, Kamb Ice Stream; RR, Raymond Ridge; UC, Unicorn; AIS, Alley Ice Stream; SD, Siple Dome.

115   data, 3) An et al. (2015) (An), which used a crust-lithosphere temperature model, and 4) Martos et al. (2017) (Martos), which inferred the GHF by compiling aeromagnetic data. The mean GHF on grounded ice is 60.78 mW m^{-2} for SR, 65.61 mW m^{-2} for Maule, 54.66 mW m^{-2} for An, and 65.49 mW m^{-2} for Martos.

2.4   Borehole temperature measurements

To validate the thermal models, we compiled all available borehole temperature profiles from Dome Fuji (Hondoh et al., 2002),
120   Styx Glacier (Yang et al., 2018), the WAIS Divide (Cuffey and Clow, 2014), the Bruce Plateau (Zagorodnov et al., 2012), Law Dome (Van Ommen et al., 1999; Dahl-Jensen et al., 1999), and the WAIS discharge to the Ross ice shelf (Engelhardt, 2004b) (Table 1). The boreholes in the West Antarctica Ice Sheet region were drilled at Whillans Ice Stream (WIS), Bindschadler Ice Stream (BIS), Engelhardt Ridge (ER), Kamb Ice Stream (KIS), Raymond Ridge (RR), Unicorn (UC), Alley Ice Stream (AIS), and Siple Dome (SD) (Engelhardt, 2004a) (Figure. 1b). We use here borehole names from Engelhardt (2004b): ER-1996-12,
125   SD-1997-1, RR-1997-42, KIS-1996-2, KIS-2000-1,2, UC-1993-11, UC-1993-14, AIS/WIS-1991-1, AIS/WIS-1995-4,7, and BIS-1998-4,5.

Name	Latitude	Longitude	Surface Temperature (°C)	Drilled Depth (m)	Ice Thickness (m)	Date	Reference
			Slow flow region				
Dome Fuji	77°19'1"S	39°42'12"E	-57.3	3035.2	3028 ± 15^{a}	1996 Dec	Hondoh et al. (2002)
SD-1997-1	81°39'30"S	211°11'30"E	-24.55		1004.6	1997 Nov	Engelhardt (2004b)
RR-1997-42	81°35'47"S	211°18'22"E	-24.55		955.0	1998 Jan	Engelhardt (2004b)
Styx Glacier	73°51'6"S	163°41'13.20"E	-31.8	210.5^{b}	550^{c}	2016 Nov	Yang et al. (2018)
UC-1993-11	83°34'56"S	221°51'15"E	-25.09		910.6	1993 Dec	Engelhardt (2004b)
UC-1993-14	83°40'45"S	221°37'42"E	-25.09	1091.6	1091.6	1994 Jan	Engelhardt (2004b)
WAIS Divide	79°28'0"S	112°4'60"W	-29.97	3405^{d}	3455^{e}	2006-2011	Slawny et al. (2014)
Law Dome	66°46'11"S	112°48'25"E	-21.8	1195.6^{f}	1220 ± 25^{g}	1996-1997	Van Ommen et al. (1999)
Bruce Plateau	66°1'12"S	295°57'36"E	-14.8	447.65^{h}	447^{h}	2010 Feb	Zagorodnov et al. (2012)
ER-1996-12	82°40'36"S	224°10'29"E	-25.85		1123.9	1997 Jan	Engelhardt (2004b)
KIS-1996-2	82°26'42"S	224°1'24"E	-26.92		1189.0	1996 Nov	Engelhardt (2004b)
KIS-2000-1,2	82°22'0"S	223°35'60"E	-25.5		949.4	2000 Dec	Engelhardt (2004b)
			Fast flow region				
WIS-1988-1	83°29'58"S	221°34'34"E	-25.52		1035.0	1988 Dec	Engelhardt (2004b)
WIS-1995-4,7	83°27'43"S	221°3'13"E	-24.94		1026.3	1997 Jan	Engelhardt (2004b)
BIS-1998-4,5	81°4'25"S	219°59'41"E	-24.35		1086.0	1999 Jan	Engelhardt (2004b)

Table 1. Summary of each borehole information. The dates refer to when the boreholes were drilled. [a]Parrenin et al. (2007); [b]Yang et al. (2018); [c]Hur (2013); [d]Slawny et al. (2014); [e]WAIS Divide Project Members (2013); [f]Morgan et al. (1997); [g]Zagorodnov et al. (2012).

Since the vertical distance between temperature measurements along the borehole profile, and triangle mesh were not uniform, we calculated a weighted absolute misfit between the modeled and measured temperatures (or modeled ice surface velocities) when evaluating the thermal model's performance:

$$\text{misfit} = \sum_{i=1}^{n_{obs}} w_i \left| Y_i^{mod} - Y_i^{obs} \right| \tag{6}$$

where n_{obs} is the number of measured points at each borehole (or the number of observed ice velocities), i indicates the index of the specific measured elevation (or index of the ice velocity area), w_i is a weight calculated from the ratio of a specific measured point's occupying length to the total measured length (or ratio of the measured area to the total area), and Y_i is the temperature (or ice velocity magnitude). The subscripts obs and mod indicate the observed and modeled variables, respectively.

To evaluate the performance of the model, a weighted correlation factor, R^2, was calculated as follows:

$$R^2 = 1 - \frac{SS_{res}}{SS_{tot}} \tag{7}$$

where SS_{res} is the sum of the squares of the residuals and SS_{tot} is the sum of the squares. SS_{res} and SS_{tot} were calculated as:

$$SS_{res} = \frac{\sum_{i=1}^{n_{obs}} w_i \left(Y_i^{mod} - Y_i^{obs} \right)^2}{\sum_{i=1}^{n_{obs}} w_i} \tag{8}$$

$$SS_{tot} = \frac{\sum_{i=1}^{n_{obs}} w_i \left(Y_i^{mod} - \overline{Y^{obs}} \right)^2}{\sum_{i=1}^{n_{obs}} w_i} \tag{9}$$

where $\overline{Y}$ is the weighted mean value of Y. Weights in SS_{res} and SS_{tot} are the same as those used in the weighted absolute misfit.

Since the ice thickness and the surface temperature of the ice flow model are not always exactly consistent with the observed borehole data, we made adjustments using an exponential decaying correction following Pattyn (2010):

$$X_{corr} = X - (X_0 - X) \exp \left(-\frac{\sqrt{(x - x_w)^2 + (y - y_w)^2}}{\sigma} \right) \tag{10}$$

where (x_w, y_w) is the location of the borehole, X_0 is the observed quantity, and X is the model ice thickness or surface temperature. The observed surface temperature is as shown in Table 1. X_{corr} is the corrected data, and σ is the radius of influence, which is here set to 50 km. The geometry from BedMachine was constrained using radar-derived ice thickness measurements, except for that at Dome Fuji, and Law Dome, for which the mapping remained largely unconstrained. These two locations are the only places where an ice thickness correction was applied so that the ice thickness is 3,090 m at Dome Fuji, and 1,220 m at Law Dome, respectively.

3 Results

3.1 Model experiments

To estimate the ice temperature of the entire Antarctic continent, we performed eight different experiments by combining two different vertical velocity profiles (IVz and IVz-nosliding) and four different GHF datasets.Table 2 shows the weighted absolute misfits between the modeled and observed surface ice velocities across the entire domain. The mean ice surface velocity misfit is 12.45 m yr^{-1} for the IVz group, and 26.33 m yr^{-1} for the IVz-nosliding group. The standard deviation of the ice velocity misfit for the IVz group, 0.09 m yr^{-1}, is relatively lower than that of the IVz-nosliding group, 3.4 m yr^{-1}.

Figure 2 displays the measured and modeled vertical profiles of the ice temperature at the 15 borehole locations. The measured vertical profiles of the borehole temperatures, marked as black dashed lines in Figure 2, can be categorized into two

The Cryosphere
Discussions

| GHF | Vertical velocity | |
	IVz	IVz-nosliding
SR	SR-IVz	SR-IVz-nosliding
	(12.43 m yr $^{-1}$)	(30.56 m yr $^{-1}$)
Maule	Maule-IVz	Maule-IVz-nosliding
	(12.46 m yr $^{-1}$)	(27.54 m yr $^{-1}$)
An	An-IVz	An-IVz-nosliding
	(12.56 m yr $^{-1}$)	(23.97 m yr $^{-1}$)
Martos	Martos-IVz	Martos-IVz-nosliding
	(12.34 m yr $^{-1}$)	(23.27 m yr $^{-1}$)

Table 2. Experimental design for eight simulations using different vertical velocities and geothermal heat fluxes. The value between parentheses under each experiment represents the weighted absolute misfit between observed and modeled surface ice velocity across the entire domain.

groups based on temperature profile shapes. One group exhibits concave profiles, for which the vertical advection toward the bed dominates, , while the other group has more linear shape, for which vertical diffusion dominates. Dome Fuji, SD-1997-1, RR-1997-42, ER-1996-12, and Styx Glacier at slow flow regions show diffusion dominant temperature profiles compared to the WAIS Divide, Bruce Plateau, Law Dome, KIS-1996-2, KIS-2000-1,2, UC-1993-11, and UC-1993-14, where the advection toward the bed dominates. Note that AIS/WIS-1991-1, AIS/WIS-1995-4,7, and BIS-1998-4,5 located in fast flow regions, have concave temperature profiles.

3.2 Borehole temperature profiles

To provide a quantitative comparison between the modeled and observed borehole temperatures, a weighted absolute misfit and R^2 were calculated (Table 3). The average temperature misfit values for IVz and IVz-nosliding are 6.61°C and 4.39°C, respectively, and 2.44°C and 2.59°C for slow and fast flow regions. The temperature misfit value of the IVz-nosliding group is lower than that of the IVZ group, however, the misfit temperatures in the fast flow regions for IVz and IVz-nosliding are not exactly the same. The spread in misfits among the different vertical velocity schemes is larger than the one obtained when varying GHF. This shows that the difference in GHF has a limited influence on estimating the overall temperature profiles, while the choice of vertical velocities has a stronger impact. Both the IVz and IVz-nosliding groups demonstrate good performance in fast flow regions, such as AIS/WIS and BIS. In the case of slow flow regions, the thermal model's performance for the IVz-nosliding group is improved compared to the IVz group, and the model produced a reduced temperature misfit and increased R^2 values, except for ER and KIS regions. A more detailed description of misfit values for each borehole can be found in the next section.

Let's first focus on the first three borehole profiles: SD, RR, and Dome Fuji. They all have linear temperature profiles, which are rarely observed in general borehole temperature profiles. SD and RR are adjacent to each other, but measurements of
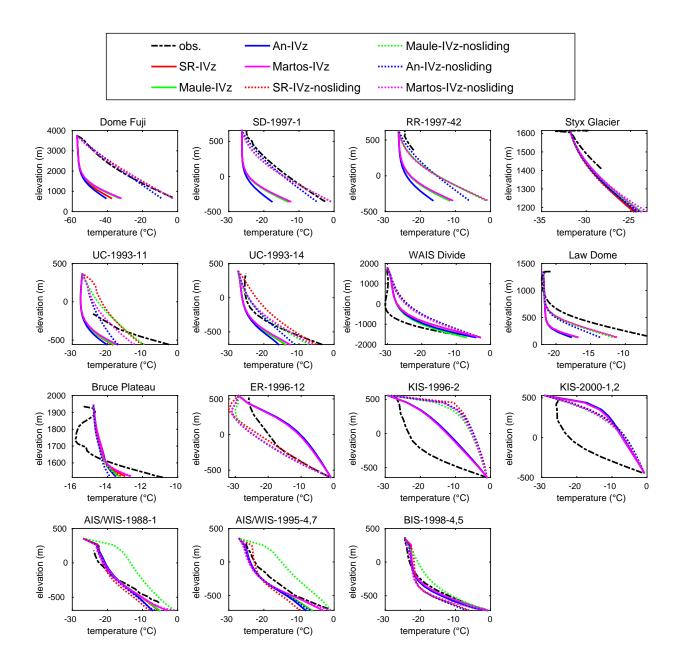
Figure 2. Observed and modeled vertical temperature profiles from eight different experiments at 15 borehole locations.

Vertical velocity	IVz				IVz-nosliding			
GHF	SR	Maule	An	Martos	SR	Maule	An	Martos
slow flow region								
Dome Fuji	19.43	18.68	19.98	18.49	1.55	1.15	1.77	**1.10**
	(-1.03)	(-0.84)	(-1.18)	(-0.79)	(0.99)	(0.99)	(0.98)	(0.99)
SD-1997-1	7.88	7.93	8.75	7.76	1.29	**1.27**	1.35	1.32
	(-0.66)	(-0.68)	(-1.14)	(-0.60)	(0.96)	(0.96)	(0.96)	(0.96)
RR-1997-42	2.47	2.47	2.49	2.46	1.56	1.53	**0.99**	1.62
	(-8.54)	(-8.54)	(-8.76)	(-8.51)	(-2.52)	(-2.39)	(-0.53)	(-2.80)
Styx Glacier	0.69	0.65	0.65	0.60	0.73	0.62	0.65	**0.57**
	(0.54)	(0.59)	(0.58)	(0.65)	(0.47)	(0.62)	(0.57)	(0.68)
UC-1993-11	15.36	15.38	15.35	15.35	**10.32**	11.94	13.62	12.85
	(-9.62)	(-9.65)	(-9.62)	(-9.61)	(-4.09)	(-5.45)	(-7.36)	(-6.50)
UC-1993-14	3.87	3.88	4.17	3.69	2.02	1.34	2.01	**1.20**
	(0.42)	(0.42)	(0.30)	(0.49)	(0.88)	(0.93)	(0.77)	(0.94)
WAIS Divide	3.29	**2.34**	2.71	3.26	5.41	5.21	5.20	4.87
	(0.44)	(0.73)	(0.65)	(0.45)	(-0.51)	(-0.45)	(-0.44)	(-0.25)
Law Dome	2.88	2.89	2.95	2.88	1.52	1.61	1.89	**1.50**
	(-0.07)	(-0.09)	(-0.14)	(-0.08)	(0.75)	(0.71)	(0.57)	(0.75)
Bruce Plateau	0.80	0.83	0.85	0.78	0.80	0.78	0.83	**0.71**
	(0.42)	(0.36)	(0.31)	(0.46)	(0.41)	(0.41)	(0.30)	(0.54)
ER-1996-12	5.12	5.17	5.26	5.00	**3.17**	3.44	3.68	3.79
	(0.36)	(0.35)	(0.33)	(0.39)	(0.69)	(0.75)	(0.72)	(0.69)
KIS-1996-2	7.35	7.46	7.47	**7.22**	13.67	12.51	12.85	13.06
	(-0.32)	(-0.36)	(-0.37)	(-0.28)	(-3.30)	(-2.67)	(-2.86)	(-2.98)
KIS-2000-1,2	10.59	10.66	10.73	10.40	10.22	**9.65**	9.92	9.83
	(-1.53)	(-1.57)	(-1.59)	(-1.44)	(-1.45)	(-1.19)	(-1.31)	(-1.28)
fast flow region								
AIS/WIS-1988-1	3.21	3.17	3.19	3.28	3.99	3.65	**2.54**	2.63
	(0.48)	(0.49)	(0.47)	(0.46)	(0.19)	(0.47)	(0.76)	(0.64)
AIS/WIS-1995-4,7	3.50	3.51	3.56	3.17	3.57	4.60	**1.15**	3.17
	(0.68)	(0.68)	(0.65)	(0.75)	(0.54)	(0.46)	(0.93)	(0.73)
BIS-1998-4,5	0.64	0.66	0.76	**0.64**	1.98	1.94	0.74	1.10
	(0.99)	(0.99)	(0.98)	(0.99)	(0.87)	(0.89)	(0.98)	(0.94)

Table 3. Weighted absolute misfit between observed and modeled borehole temperatures according to each experiment. Bold text indicates the minimum misfit values from among eight experiments at each borehole. The values in parentheses underneath the misfit values are the R^2 values.

Borehole Name	IVz					IVz-nosliding				
	SR	Maule	An	Martos	mean	SR	Maule	An	Martos	mean
slow flow region										
Dome Fuji	-0.14	-0.14	-0.14	-0.14	-0.14	-0.01	-0.01	-0.00	-0.01	-0.01
SD-1997-1	-0.41	-0.41	-0.40	-0.41	-0.41	-0.08	-0.08	-0.04	-0.08	-0.07
RR-1997-42	-0.13	-0.12	-0.12	-0.13	-0.12	-0.09	-0.09	-0.04	-0.10	-0.08
Styx Glacier	-0.29	-0.30	-0.27	-0.33	-0.30	-0.08	-0.08	-0.08	-0.09	-0.08
UC-1993-11	-0.19	-0.21	-0.17	-0.22	-0.20	0.13	0.10	0.11	0.08	0.11
UC-1993-14	-0.45	-0.46	-0.43	-0.47	-0.45	-1.68	-0.28	-0.68	-0.67	-0.83
WAIS Divide	0.02	0.03	0.03	0.02	0.03	0.20	0.21	0.21	0.19	0.20
Law Dome	-1.51	-1.53	-1.47	-1.56	-1.52	-0.03	-0.01	0.02	-0.03	-0.01
Bruce Plateau	-5.25	-5.32	-5.26	-5.41	-5.31	-3.55	-2.55	-3.07	-3.17	-3.08
ER-1996-12	-0.23	-0.23	-0.23	-0.23	-0.23	-0.30	-0.22	-0.23	-0.26	-0.25
KIS-1996-2	0.04	0.04	0.05	0.04	0.04	-0.07	-0.06	-0.07	-0.08	-0.07
KIS-2000-1,2	0.29	0.28	0.30	0.27	0.29	0.03	0.03	0.03	0.02	0.03
fast flow region										
AIS/WIS-1988-1	0.27	0.27	0.29	0.24	0.27	0.52	-0.06	0.40	0.34	0.30
AIS/WIS-1995-4,7	0.35	0.35	0.36	0.33	0.35	0.50	0.16	0.33	0.27	0.32
BIS-1998-4,5	2.52	2.86	1.58	3.47	2.61	-0.04	-1.16	-2.19	-2.22	-1.40

Table 4. Depth-averaged vertical velocity for each experiment at each borehole. Positive values indicate upward advection.

borehole temperatures at RR are limited to the top few hundred meters. Dome Fuji is located in the interior of the ice sheet. For these boreholes, IVz-nosliding group does not capture the linear shape of the temperature profiles. The IVz-nosliding group at these boreholes has a misfit value within 2°C (Table 3). In addition, the R^2 value of the IVz-nosliding group is higher than that

185 of IVz group. The basal temperatures from the IVz-nosliding group reach the pressure melting point at SD, RR (Engelhardt, 2004b), and Dome Fuji. In the case of An, the GHF at each borehole is 40.1 mW m^{-2} for Dome Fuji, 64.9 mW m^{-2} for SD, and 65.3 mW m^{-2} for RR, which are lower than the values from other GHF sources. The basal modeled temperature at An is the lowest, and does not reach pressure melting point. The depth-averaged vertical velocity at Dome Fuji is -0.14 m yr^{-1} for IVz (where a negative value means the vector is oriented downward), which is a higher value than that of IVz-nosliding (-0.01

190 m yr^{-1}) (Table 4). The depth-averaged vertical velocities of IVz at SD and RR are also higher than that of IVz-nosliding. This suggests a larger advection toward the ice sheet base in the IVz group, where downward heat advection is more dominant than the diffusion process, and leads to a colder basal temperature compared to the ones in the IVz-nosliding group.

The borehole of Styx Glacier is a shallow ice core limited to 210.5 m (Yang et al., 2018), even though the ice thickness from ice penetrating radar is approximately 550 m (Hur, 2013). Both IVz and IVz-nosliding groups display similar average misfit

195 values of ∼0.64°C, which shows good agreement with the observed temperature profile. The thermal model results suggest that we do not reach the melting point at the borehole of Styx Glacier in all experiments.

The measured UC borehole temperature profile displays a relatively high basal temperature gradient compared to the other adjacent boreholes, such as AIS/WIS boreholes (Engelhardt, 2004b). The mean GHF in the UC region is approximately 81.4 mW m^{-2} for SR, 86.5 mW m^{-2} for Maule, 62.8 mW m^{-2} for An, and 95.6 mW m^{-2} for Martos. The current modeled
200 temperature profiles at UC-1993-11 and UC-1993-14 agree well with the measured temperature regardless of the choice of GHFs. The misfit value for the modeled and observed temperatures from the IVz-nosliding group is lower than that of the IVz group. In addition, the misfit of UC-1993-14 for IVz-nosliding is lower than that of UC-1993-11 (Table 3). UC-1993-14 is located in a slow region; however, UC-1993-11 is adjacent to the shear margin of the AIS ice stream, which induces a sharp transition in the basal velocity constraints for the IVz-nosliding group where the ice velocity crosses 10 m yr^{-1}. While the
205 IVz-nosliding group captures better the observed temperature profiles for UC-1993-14, it is not the case for UC-1993-11.

The modeled basal temperature at the WAIS Divide reaches the pressure melting point only for the SR and Martos IVz groups. The GHF is approximately 112.6 mW m^{-2} for SR, and 141 mW m^{-2} for Martos; these values are higher than those of the other two GHF datasets, which are 60.3 mW m^{-2} for Maule and 68.9 mW m^{-2} for An. The basal melting rate of the IVz-nosliding group is 7.7 mm yr^{-1} for SR, 2.2 mm yr^{-1} for Maule, 3.2 mm yr^{-1} for An, and 10.9 mm yr^{-1} for Martos.
210 GHF estimations in previous studies are 113.3±16.9 mW m^{-2} from Talalay et al. (2020) and 90.5 mW m^{-2} from Mony et al. (2020). The thickness at WAIS Divide is 3455 m (WAIS Divide Project Members, 2013). However, the drilling depth is 3405 m (Slawny et al., 2014), and does not reach the bed, so we do not know the rate of basal melting. According to Talalay et al. (2020), the estimated basal temperature at WAIS Divide reaches the pressure melting point, and the basal melting rate is about 3.7 ± 1.7 mm yr^{-1}. All experiments show reasonably good agreement in terms of the shape of the observed borehole
215 temperature profile at WAIS Divide regardless of the choice of GHF. The average misfit value of the borehole temperature and the R^2 value for IVz are 2.90°C and 0.56, respectively, and these values are better than those of IVz-nosliding (Table 3).

At Law Dome, the misfit between the observed and modeled temperatures is 2.9°C and 1.63°C for the IVz and IVz-nosliding groups, respectively. The mean R^2 value for IVz-nosliding is 0.7, which is higher than that of IVz with a value of -0.1 (Table 3). A primary difference between IVz and IVz-nosliding is the depth-averaged vertical velocity, which of value is -1.5 m yr^{-1}
220 for IVz group and -0.1 m yr^{-1} for IVz-nosliding (Table 4). In the Law Dome case, we confirm that the use of IVz-nosliding improves the model's vertical temperature profile (Figure 2).

The observed ice velocity at Bruce Plateau is 45 m yr^{-1} according to Mouginot et al. (2012), which is higher than the previously reported value of 10 ± 4 m yr^{-1} (Zagorodnov et al., 2012). We find that none of the modeled thermal profiles can reproduce the upper part of the observed ice temperature that captured the colder surface temperature of past climate
225 (Zagorodnov et al., 2012). The mean vertical velocity for the IVz group is -5.31 m yr^{-1}, and -2.93 m yr^{-1} for the IVz-nosliding group; these values indicates high vertical advection toward the bottom.

Except for ER-1997-12, neither IVz nor IVz-nosliding group capture the observed temperature profiles at the KIS boreholes. All modeled temperature profiles exhibit a convex shape (Figure 2). At ER-1997-12, the mean misfit between the modeled and observed temperature is 3.5°C for the IVz-nosliding group and 5.1∘C for the IVz group (Table 3).

230 The AIS/WIS and BIS boreholes are located in fast flow regions where the ice velocities are 369 m yr^{-1} for AIS/WIS-1991-1, 379 m yr^{-1} for AIS/WIS-1995-4,7, and 220 m yr^{-1} for BIS-1998-4,5. In these regions, both IVz and IVz-nosliding allow

for basal sliding, and the vertical velocities calculated for the IVz-nosliding and IVz groups are not significantly different, as expected. The modeled temperature profiles for IVz and IVz-nosliding show similar results. The average misfit value of the IVz group is 3.21°C for AIS/WIS-1988-1, 3.44°C for AIS/WIS-1995-4,7, and 0.67°C for BIS-1998-4,5 (Table 3). The misfit

235 value of the modeled and observed temperatures at BIS is lower than that of AIS/WIS. The primary difference between the BIS and AIS/WIS regions is that the bed geometry in the BIS region was constructed using a mass conservation approach, which relies on the equation of ice incompressibility. In contrast, the bed geometry in the AIS/WIS region was constructed using the stream diffusion method, which produces bed topography similar to kriging (Figure S4). This suggests that enhancement in the quality of the geometry and utilizing the mass conservation method in the fast flow regions would improve the estimation of

240 the vertical velocity by the IVz equation with sliding as well as the overall performance of the thermal model. The AIS/WIS-1995-4,7 borehole is located at the center of the ice stream, whereas AIS/WIS-1988-1 is relatively near the margin of the ice stream. Although the bed geometry at AIS/WIS was constructed using the kriging method, IVz reproduces the temperature profile reasonably well at the center of fast ice flow regions.

3.3 Subglacial conditions

245 Figure 3a and 3b show the mean and standard deviation of the basal temperature distribution for the eight experiments. The mean basal temperature in the peripheral region, where the ice discharges to the ocean, reaches the ice pressure melting point. The standard deviation of the basal temperature is higher in the internal ice compared to the peripheral regions. In the case of IVz-nosliding, constraining the basal velocity to zero in slow flow regions leads to a warmer basal temperature distribution compared to the IVz group. In slow flow regions, the basal temperature of the IVz group shows a notable difference depending

250 on the choice of GHF. The modeled basal temperatures in the Maule and Martos experiments, which have higher mean GHF values (Table 5), are warmer than those in SR and An experiments, as expected. The mean GHF of An is the lowest compared to the other GHFs, and therefore, the basal temperature at each borehole modeled with the An GHF is lower than those of the other GHFs.

All the experiments generally indicate that most of the regions experiencing basal melting are concentrated in fast flow

255 regions, where basal frictional heat is significant and provides enough heat for the ice to reach the pressure melting point (Figure 4). Since IVz-nosliding displays lower vertical advection than that of IVz, the basal temperature of the IVz-nosliding group in slow flow regions is warmer than that of IVz (Figure 4e-l).

The mean total grounded ice melting rate is 26.62 Gt yr^{-1} for the IVz group, and 30.21 Gt yr^{-1} for the IVz-nosliding group (Table 5). The total grounded ice melting rate for the IVz-nosliding group is 3.59 Gt yr^{-1} higher than that of IVz. The surplus

260 of the mean total basal melting rate of the IVz-nosliding group is supplied by 2.51 Gt yr^{-1} (70%) and 1.08 Gt yr^{-1} (30%) in the slow and fast flow regions, respectively. The total melting fraction of the grounded ice, which represents the grounded ice melting area, is 53.60% for the IVz group, and 61.59% for the IVz-nosliding group (Table 5). Each basin displays significant differences in terms of the grounded ice melting rate depending on the GHF source. Martos provides a high GHF along the West Antarctic Rift System, and therefore, Martos' total grounded ice melting rate in basins 8 and 10 has the highest values

265 of 9.33 Gt yr^{-1} and 9.99 Gt yr^{-1} for IVz and IVz-nosliding, respectively. Basin 5, including Totten, Moscow University, and
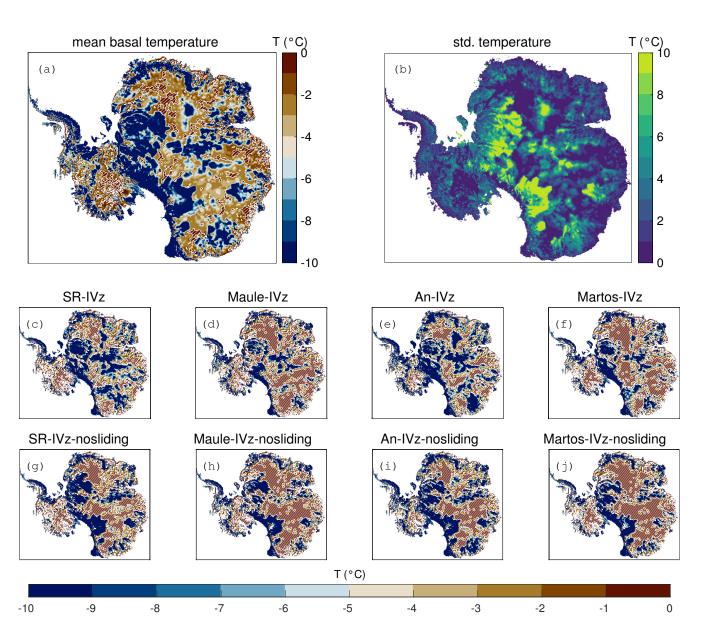
Figure 3. (a) Mean and (b) standard deviation of the basal temperature distribution from eight experiments. (c-j) Basal temperature distribution for each experiment. The temperature legend is truncated below -10 °C. White slash line region indicates that the basal temperature of ice reaches the pressure melting point.
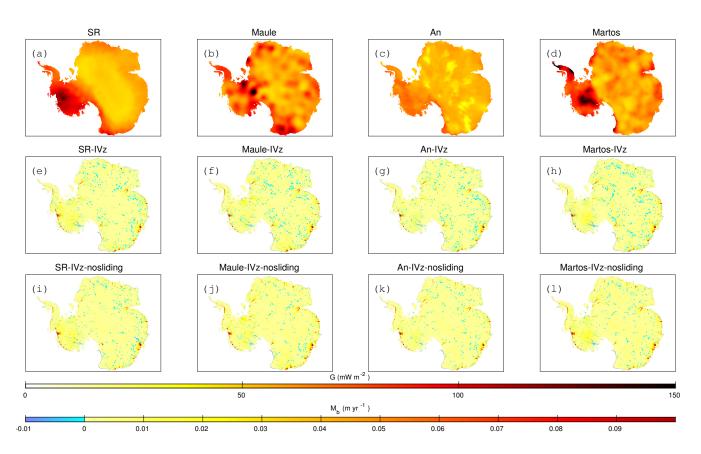
Figure 4. Upper panels (a-d) are the geothermal heat flux distributions of each source. Lower panels (e-l) are the basal melting rate distributions.

Holmes Glacier, shows the highest total grounded ice melting rate in East Antarctica, excluding basins 8 and 15. The GHF from An, which is the lowest value among all GHFs, shows the lowest total grounded ice melting rate.

4 Discussion

Previous studies that have successfully reproduced borehole temperature profiles using one-dimensional thermal analytical
270 solutions have been limited to slow flow regions (Joughin et al., 2003; Mony et al., 2020; Talalay et al., 2020). These studies
have demonstrated good agreement between modeled and observed temperatures, which is expected given their simplicity and
tunability of the analytical solutions. One important tunable parameter is the analytical vertical velocities, which rely on ice
surface mass balance (Hindmarsh, 1999; Joughin et al., 2003; Talalay et al., 2020). The choice of vertical velocity is a key
factor in reproducing borehole temperature profiles. Uncertainties in the GHF have also been identified as a major factor in
275 reproducing observed borehole temperature profiles (Talalay et al., 2020; Mony et al., 2020). On the other hand, some other
studies have shown that uncertainties in the GHF have little influence on model performance in terms of ice dynamics (Larour

15

	vertical velocity	Grounded ice melting rate (Gton yr^{-1})							
		IVz				IVz-nosliding			
	GHF	SR	Maule	An	Martos	SR	Maule	An	Martos
	basin id								
East Antarctica	1	1.16	1.36	0.82	1.07	1.06	1.70	1.14	1.42
	2	0.71	0.89	0.72	0.93	0.78	1.26	0.99	1.22
	3	1.64	2.27	1.60	2.18	1.42	2.56	1.75	2.27
	4	1.65	2.46	1.64	2.13	1.79	3.18	2.13	2.55
	5	3.65	4.40	3.68	4.73	3.83	5.09	3.99	5.04
	6	1.95	3.32	1.49	1.85	1.69	3.64	1.60	1.88
	7	0.39	0.63	0.26	0.25	0.41	0.71	0.35	0.32
	16	0.21	0.41	0.18	0.35	0.24	0.63	0.31	0.50
Ross ice shelf	8	3.98	3.53	2.65	5.04	4.41	4.26	3.14	5.55
West Antarctica	9	1.06	0.82	0.80	0.84	1.28	1.23	1.18	1.21
	10	5.09	3.59	3.44	4.29	4.35	4.08	3.95	4.44
	11	0.33	0.23	0.25	0.27	0.39	0.36	0.38	0.39
Antarctic Peninsula	12	0.76	0.81	0.72	0.90	0.82	1.18	1.00	1.15
	13	0.03	0.02	0.02	0.04	0.02	0.01	0.01	0.04
	14	0.00	0.01	0.00	0.02	0.02	0.03	0.02	0.05
Ronne-Filchner ice shelf	15	3.14	5.12	2.93	4.73	2.73	5.55	3.10	4.98
Total grounded ice melting rate (Gton yr^{-1})		25.78	29.86	21.21	29.64	25.23	35.49	25.04	33.01
grounded ice melting fraction (%)		48.29	61.70	45.39	59.01	58.35	66.28	55.29	66.42
mean GHF (mW m^{-2})		60.78	65.61	54.66	65.49	60.78	65.61	54.66	65.49

Table 5. Grounded ice basal melting rates of eight experiments at each basin (Figure 1) as well as the total grounded ice melting rate and the total grounded melting fraction corresponding to each experiment.

et al., 2012a; Smith-Johnsen et al., 2020a), and simulating future projections (Schlegel et al., 2018; Smith-Johnsen et al., 2020b; Seroussi et al., 2013). Therefore, to test other factors, such as different GHFs and vertical velocities, that may affect the calculation of borehole temperatures, we used a three-dimensional thermo-mechanical model in order to account for both

280   horizontal and vertical advection. We compared our calculated temperatures to observed borehole profiles in both fast and slow flow regions.

In slow flow regions, we find that IVz-nosliding experiments show a reasonably good agreement with the observed borehole temperature profiles. However, the three-dimensional thermal model occasionally estimates convex temperature profiles, which are not consistent with the observations, such as KIS-1996-2 and KIS-2000-1,2 boreholes. Compared to other boreholes, the

285   ice velocities at KIS and ER gradually decrease from upstream to downstream and KIS boreholes, and coincide with the

presence of a basal ridge (Figure S1). Additional regional modeling is required to better understand temperature profiles at KIS boreholes.

In fast flow regions, Joughin et al. (2004) utilized a thermal model with vertical velocity derived from an analytical solution, which reproduced the observed borehole temperature profile of BIS-1998-4,5 with good agreement (UpD in Joughin et al.
290   (2004)). Here, we also find that the modeled temperature using a vertical velocity based on the equation of incompressibility without any constraint or tunable parameter also agrees well with the observed temperatures in this sector.

The total grounded ice melting rate for both the IVz and IVz-nosliding groups falls within the range reported by previous studies. It is lower than 65 Gt yr^{-1} from Pattyn (2010) and higher than 16 Gt yr^{-1} from Llubes et al. (2006). In the study by Joughin et al. (2009), they adopted a homogeneous GHF value of 70 mW m^{-2}, which is similar to the mean GHFs from Maule,
295   66.95 mW m^{-2}, and An, 67.15 mW m^{-2} at basin 10, which includes Pine Island and Thwaites Glaciers (see basin in Figure 1). However, the total grounded ice melting rate estimated by Joughin et al. (2009), 5.2 Gt yr^{-1}, is higher than that of IVz group (average value of Maule and An), 3.5 Gt yr^{-1}, and IVz-nosliding group (average value of Maule and An), 3.7 Gt yr^{-1}. Joughin et al. (2009) assumed that the vertical velocity varied linearly from the surface mass balance at the surface to zero at the bed in fast flow regions, and they relied on an analytical solution similar to the one presented by Hindmarsh (1999) in slow
300   flow regions (Dansgaard and Johnsen, 1969; Dahl-Jensen et al., 1999). Since Joughin et al. (2009) used an analytical solution that underestimated the magnitude of the vertical velocity compared to the vertical velocity obtained from the equation of ice incompressibility, it results in overestimation of the total grounded ice melting rate in basin 10.

Thermal models have been used to estimate the melting rate beneath grounded ice taking into account the activity and connectivity between subglacial lakes identified through conventional and swath altimetry data (Smith et al., 2017). In this
305   study, we confirm that using the equation of ice incompressibility to reconstruct the ice vertical velocity provides a viable way of computing a temperature profiles that exhibit goods agreement with observations in fast flow regions, such as the BIS region. Given that the geometry of fast flow regions, such as Thwaites Glacier, was generated using the mass conservation method (Morlighem et al., 2020), this study provides reliable melting rates that could be used to understand the subglacial hydrology system of this sector.

310   We find that the impact of using different GHF fields has only a modest influence on the ice temperature field and the total grounded ice basal melting rate. Under these circumstances, our results reveal that the shapes of the borehole temperature profile are less sensitive to the current estimated GHFs than previously reported. It is also worth noting that the initialization with the GHF from An results in underestimated basal temperatures and a lower total grounded ice melting rate due to an excessively low GHF value compared to other datasets.

315   The IVz-nosliding experiment has the advantage of better simulating the vertical temperature profiles in slow flow regions compared to IVz. However, it tends to produce large discrepancies between modeled and observed surface ice velocities (Figure S3). For instance, the An-IVz-nosliding thermal model experiments exhibit the largest misfits in ice velocity among all the experiments, as the lowest value of average GHF leads to relatively high ice rigidity that perturbs the ice flow in the slow flow regions. In contrast, IVz experiment shows relatively smaller misfit values in surface ice velocity because sliding
320   compensates for the underestimated internal deformations in the slow flow region. In general, we find that IVz leads to a higher

depth-averaged ice rigidity compared to IVz-nosliding in slow regions due to presence of colder ice temperatures (Figure S2). Higher ice rigidity causes ice to deform less vertically, through vertical shear, and the surface ice velocity with no-sliding cannot reproduce the observed surface velocities. In other words, the surface ice velocity of IVz-nosliding shows a larger ice velocity misfit compared to that of the IVz group, because the basal velocities are constrained to zero and cannot compensate

325 for the high velocity misfit.

In slow flow regions, a competition between vertical diffusion and advection determines the shape of the temperature profiles and the bottom temperatures. In the IVz experiments, the boundary condition for basal vertical velocity is recovered with the gradient of the bed geometry and the basal melting rate. This approach provides relatively high vertical velocities in slow flow regions. The vertical velocities are not always in agreement with the analytical expression of vertical velocities assuming a

330 stationary bed and no-sliding. As the depth-averaged vertical velocity of IVz is higher than that of IVz-nosliding, cold surface temperatures can be more effectively transferred deeper into the ice column.

Finally, borehole temperatures have a long-term memory of past climate air temperatures and are a good proxy for recon-struction over a few hundred years or longer using inverse modeling (Nagornov et al., 2001; Zagorodnov et al., 2012). This history is not accounted for in this study as we assumed thermal steady state using current climatological information. Despite

335 this strong limitation, we find that this approach provides temperature profiles that are in good agreement with observations.

5 Conclusions

In this study, we used a three-dimensional thermo-mechanical model of Antarctica with different sources of GHF and vertical velocity fields to reproduce different thermal states of the Antarctic ice sheet, and we compared the results to 15 in situ measured borehole temperature profiles in slow and fast flow regions. Comparing the modeled to measured borehole temperature profiles,

340 we confirmed that the vertical ice velocitiy based on the equation of incompressibility (IVz) is suitable for fast flow regions, such as BIS, where the bed geometry is constructed with using the mass conservation method, while an IVz that ignores basal sliding (IVz-nosliding) performs better in slow flow regions. Our results show that the vertical temperature profile and basal conditions are more sensitive to the vertical velocity field than the GHF. The effects of different GHFs have little influence on the variance in basal temperature fields and the grounded ice melting rate compared to the vertical velocities. However, the

345 total grounded ice melting rate and average basal temperature are proportional to the magnitude of the average GHF values for the same vertical velocity method. Finally, constraining the basal velocity to zero in slow moving regions is a reasonable assumption and leads to a more realistic temperature profile.

Code and data availability. ISSM is open source and can be download at https://issm.jpl.nasa.gov. Law Dome temperature profile by Van Ommen et al. (1999) is available online (doi:10.26179/5dca396372c0c). Dome Fuji temperature profile is available at Hondoh et al.

350 (2002). Styx Glacier borehole temperature profile by Yang et al. (2018) is obtained with personal communication. Bruce Plateau temper-ature profile is available at Zagorodnov et al. (2012). WAIS Divide borehole temperature by Cuffey and Clow (2014) is available online (http://dx.doi.org/10.7265/N5V69GJW). SD, RR, UC, ER, KIS, AIS/WIS, BIS borehole temperature by Engelhardt (2004b) are available

online (http://dx.doi.org/10.7265/N5PN93J8). GHF map by Shapiro and Ritzwoller (2004) and Maule et al. (2005) are available at ALBMAP

v1.0 (doi.pangaea.de/10.1594/PANGAEA.734145). GHF map by An et al. (2015) is available at http://www.seismolab.org/model/antarctica/lithosphere/index.html.

355   GHF map by Martos et al. (2017) is available at online (https://doi.pangaea.de/10.1594/PANGAEA.882503). 2m air temperature by Dee et al.
(2011) is available at online (https://www.ecmwf.int/en/forecasts/datasets/reanalysis-datasets/era-interim). Ice velocity map by Mouginot
et al. (2012) is available at https://nsidc.org/data/nsidc-0484/versions/2. Bed geometry of Antarctica by Morlighem et al. (2020) is available at
https://nsidc.org/data/NSIDC-0756/versions/1. Surface elevation map by Howat et al. (2019) is available at https://www.pgc.umn.edu/data/rema/.

The Cryosphere
Discussions

References

365 Alley, K. E., Scambos, T. A., Siegfried, M. R., and Fricker, H. A.: Impacts of Warm Water on Antarctic Ice Shelf Stability through Basal
Channel Formation, Nature Geoscience, 9, 290–293, https://doi.org/10.1038/ngeo2675, 2016.

An, M., Wiens, D. A., Zhao, Y., Feng, M., Nyblade, A., Kanao, M., Li, Y., Maggi, A., and Lévêque, J.-J.: Temperature, Lithosphere-
asthenosphere Boundary, and Heat Flux beneath the Antarctic Plate Inferred from Seismic Velocities, Journal of Geophysical Research:
Solid Earth, 120, 8720–8742, 2015.

370 Anker, P. G. D., Makinson, K., Nicholls, K. W., and Smith, A. M.: The BEAMISH Hot Water Drill System and Its Use on the Rutford Ice
Stream, Antarctica, Annals of Glaciology, 62, 233–249, https://doi.org/10.1017/aog.2020.86, 2021.

Aschwanden, A., Bueler, E., Khroulev, C., and Blatter, H.: An Enthalpy Formulation for Glaciers and Ice Sheets, Journal of Glaciology, 58,
441–457, https://doi.org/10.3189/2012JoG11J088, 2012.

Augustin, L. and Antonelli, A.: The EPICA Deep Drilling Program, 2002.

375 Brondex, J., Gillet-Chaulet, F., and Gagliardini, O.: Sensitivity of Centennial Mass Loss Projections of the Amundsen Basin to the Friction
Law, The Cryosphere, 13, 177–195, https://doi.org/10.5194/tc-13-177-2019, 2019.

Budd, WF., Keage, PL., and Blundy, NA.: Empirical Studies of Ice Sliding, Journal of glaciology, 23, 157–170, 1979.

Cuffey, K. M. and Clow, G. D.: Temperature Profile of the West Antarctic Ice Sheet Divide Deep Borehole,
https://doi.org/10.7265/N5V69GJW, 2014.

380 Cuffey, K. M. and Paterson, W. S. B.: The Physics of Glaciers, Academic Press, 2010.

Dahl-Jensen, D., Morgan, V. I., and Elcheikh, A.: Monte Carlo Inverse Modelling of the Law Dome (Antarctica) Temperature Profile, Annals
of Glaciology, 29, 145–150, 1999.

Dansgaard, W. and Johnsen, S. J.: A Flow Model and a Time Scale for the Ice Core from Camp Century, Greenland, Journal of Glaciology,
8, 215–223, https://doi.org/10.3189/S0022143000031208, 1969.

385 DeConto, R. M. and Pollard, D.: Contribution of Antarctica to Past and Future Sea-Level Rise, Nature, 531, 591–597,
https://doi.org/10.1038/nature17145, 2016.

Dee, D. P., Uppala, S. M., Simmons, A. J., Berrisford, P., Poli, P., Kobayashi, S., Andrae, U., Balmaseda, M. A., Balsamo, G., Bauer,
P., Bechtold, P., Beljaars, A. C. M., van de Berg, L., Bidlot, J., Bormann, N., Delsol, C., Dragani, R., Fuentes, M., Geer, A. J., Haim-
berger, L., Healy, S. B., Hersbach, H., Hólm, E. V., Isaksen, L., Kållberg, P., Köhler, M., Matricardi, M., McNally, A. P., Monge-Sanz,
390 B. M., Morcrette, J.-J., Park, B.-K., Peubey, C., de Rosnay, P., Tavolato, C., Thépaut, J.-N., and Vitart, F.: The ERA-Interim Reanalysis:
Configuration and Performance of the Data Assimilation System, Quarterly Journal of the Royal Meteorological Society, 137, 553–597,
https://doi.org/10.1002/qj.828, 2011.

Derkacheva, A., Mouginot, J., Millan, R., Maier, N., and Gillet-Chaulet, F.: Data Reduction Using Statistical and Regression Approaches for
Ice Velocity Derived by Landsat-8, Sentinel-1 and Sentinel-2, Remote Sensing, 12, 1935, https://doi.org/10.3390/rs12121935, 2020.

395 Doyle, S. H., Hubbard, B., Christoffersen, P., Young, T. J., Hofstede, C., Bougamont, M., Box, J. E., and Hubbard, A.: Physical Conditions
of Fast Glacier Flow: 1. Measurements From Boreholes Drilled to the Bed of Store Glacier, West Greenland, Journal of Geophysical
Research: Earth Surface, 123, 324–348, https://doi.org/10.1002/2017JF004529, 2018.

Engelhardt, H.: Ice Temperature and High Geothermal Flux at Siple Dome, West Antarctica, from Borehole Measurements, Journal of
Glaciology, 50, 251–256, https://doi.org/10.3189/172756504781830105, 2004a.

400   Engelhardt, H.: Thermal Regime and Dynamics of the West Antarctic Ice Sheet, Annals of Glaciology, 39, 85–92,
        https://doi.org/10.3189/172756404781814203, 2004b.

Fisher, A. T., Mankoff, K. D., Tulaczyk, S. M., Tyler, S. W., Foley, N., and and the WISSARD Science Team: High Geothermal Heat Flux
        Measured below the West Antarctic Ice Sheet, Science Advances, 1, e1500 093, https://doi.org/10.1126/sciadv.1500093, 2015.

Fox-Kemper, B., Hewitt, H. T., Xiao, C., Aðalgeirsdóttir, G., Drijfhout, S. S., Edwards, T. L., Golledge, N. R., Hemer, M., Kopp, R. E.,
405   Krinner, G., Mix, A., Notz, D., Nowicki, S., Nurhati, I. S., Ruiz, L., Sallée, J.-B., Slangen, A. B. A., and Yu, Y.: Ocean, Cryosphere and
        Sea Level Change. In Climate Change 2021: The Physical Science Basis. Contribution of Working Group I to the Sixth Assessment Report
        of the Intergovernmental Panel on Climate Change, Cambridge University Press. In Press, 2021.

Gillet-Chaulet, F.: Assimilation of Surface Observations in a Transient Marine Ice Sheet Model Using an Ensemble Kalman Filter, The
        Cryosphere, 14, 811–832, https://doi.org/10.5194/tc-14-811-2020, 2020.

410   Gillet-Chaulet, F., Hindmarsh, R. C. A., Corr, H. F. J., King, E. C., and Jenkins, A.: *In-Situ* Quantification of Ice Rheology and Direct
        Measurement of the Raymond Effect at Summit, Greenland Using a Phase-Sensitive Radar: *IN-SITU* QUANTIFICATION OF ICE RHE-
        OLOGY, Geophysical Research Letters, 38, n/a–n/a, https://doi.org/10.1029/2011GL049843, 2011.

Gillet-Chaulet, F., Gagliardini, O., Seddik, H., Nodet, M., Durand, G., Ritz, C., Zwinger, T., Greve, R., and Vaughan, D. G.: Greenland Ice
        Sheet Contribution to Sea-Level Rise from a New-Generation Ice-Sheet Model, The Cryosphere, 6, 1561–1576, https://doi.org/10.5194/tc-
415   6-1561-2012, 2012.

Glen, J. W.: The Creep of Polycrystalline Ice, Proceedings of the Royal Society of London. Series A. Mathematical and Physical Sciences,
        228, 519–538, 1955.

Hindmarsh, R. C.: On the Numerical Computation of Temperature in an Ice Sheet, Journal of Glaciology, 45, 568–574, 1999.

Hondoh, T., Shoji, H., Watanabe, O., Salamatin, A. N., and Lipenkov, V. Y.: Depth–Age and Temperature Prediction at Dome Fuji Station,
420   East Antarctica, Annals of Glaciology, 35, 384–390, 2002.

Howat, I. M., Porter, C., Smith, B. E., Noh, M.-J., and Morin, P.: The Reference Elevation Model of Antarctica, The Cryosphere, 13, 665–674,
        https://doi.org/10.5194/tc-13-665-2019, 2019.

Hubbard, B., Philippe, M., Pattyn, F., Drews, R., Young, T. J., Bruyninx, C., Bergeot, N., Fjøsne, K., and Tison, J.-L.: High-Resolution
        Distributed Vertical Strain and Velocity from Repeat Borehole Logging by Optical Televiewer: Derwael Ice Rise, Antarctica, Journal of
425   Glaciology, 66, 523–529, https://doi.org/10.1017/jog.2020.18, 2020.

Hur, SD.: Development of Core Technology for Ice Core Drilling and Ice Core Bank, Korea Polar Research Institute, Incheon, 398, 2013.

Joughin, I., Tulaczyk, S., MacAyeal, D. R., and Engelhardt, H.: Melting and Freezing beneath the Ross Ice Streams, Antarctica, Journal of
        Glaciology, 50, 96–108, https://doi.org/10.3189/172756504781830295, 2004.

Joughin, I., Tulaczyk, S., Bamber, J. L., Blankenship, D., Holt, J. W., Scambos, T., and Vaughan, D. G.: Basal Conditions for Pine Is-
430   land and Thwaites Glaciers, West Antarctica, Determined Using Satellite and Airborne Data, Journal of Glaciology, 55, 245–257,
        https://doi.org/10.3189/002214309788608705, 2009.

Joughin, I. R., Tulaczyk, S., and Engelhardt, H. F.: Basal Melt beneath Whillans Ice Stream and Ice Streams A and C, West Antarctica,
        Annals of Glaciology, 36, 257–262, https://doi.org/10.3189/172756403781816130, 2003.

Jourdain, N. C., Asay-Davis, X., Hattermann, T., Straneo, F., Seroussi, H., Little, C. M., and Nowicki, S.: A Protocol for Calculating Basal
435   Melt Rates in the ISMIP6 Antarctic Ice Sheet Projections, The Cryosphere, 14, 3111–3134, https://doi.org/10.5194/tc-14-3111-2020,
        2020.

Khazendar, A., Rignot, E., and Larour, E.: Larsen B Ice Shelf Rheology Preceding Its Disintegration Inferred by a Control Method, Geophysical Research Letters, 34, L19 503, https://doi.org/10.1029/2007GL030980, 2007.

Kingslake, J., Hindmarsh, R. C., Aḥalgeirsdóttir, G., Conway, H., Corr, H. F., Gillet-Chaulet, F., Martín, C., King, E. C., Mulvaney, R.,
440 and Pritchard, H. D.: Full-Depth Englacial Vertical Ice Sheet Velocities Measured Using Phase-Sensitive Radar, Journal of Geophysical Research: Earth Surface, 119, 2604–2618, 2014.

Kleiner, T., Rückamp, M., Bondzio, J. H., and Humbert, A.: Enthalpy Benchmark Experiments for Numerical Ice Sheet Models, The Cryosphere, 9, 217–228, https://doi.org/10.5194/tc-9-217-2015, 2015.

Larour, E., Morlighem, M., Seroussi, H., Schiermeier, J., and Rignot, E.: Ice Flow Sensitivity to Geothermal Heat Flux of Pine Island Glacier,
445 Antarctica, Journal of Geophysical Research: Earth Surface, 117, n/a–n/a, https://doi.org/10.1029/2012JF002371, 2012a.

Larour, E., Seroussi, H., Morlighem, M., and Rignot, E.: Continental Scale, High Order, High Spatial Resolution, Ice Sheet Modeling Using the Ice Sheet System Model (ISSM), Journal of Geophysical Research: Earth Surface, 117, n/a–n/a, https://doi.org/10.1029/2011JF002140, 2012b.

Llubes, M., Lanseau, C., and Rémy, F.: Relations between Basal Condition, Subglacial Hydrological Networks and Geothermal Flux in
450 Antarctica, Earth and Planetary Science Letters, 241, 655–662, https://doi.org/10.1016/j.epsl.2005.10.040, 2006.

MacAyeal, D. R.: A Tutorial on the Use of Control Methods in Ice-Sheet Modeling, Journal of Glaciology, 39, 91–98, 1993.

Martos, Y. M., Catalán, M., Jordan, T. A., Golynsky, A., Golynsky, D., Eagles, G., and Vaughan, D. G.: Heat Flux Distribution of Antarctica Unveiled, Geophysical Research Letters, 44, 11,417–11,426, https://doi.org/10.1002/2017GL075609, 2017.

Maule, C. F., Purucker, M. E., Olsen, N., and Mosegaard, K.: Heat Flux Anomalies in Antarctica Revealed by Satellite Magnetic Data,
455 Science, 309, 464–467, https://doi.org/10.1126/science.1106888, 2005.

Mony, L., Roberts, J. L., and Halpin, J. A.: Inferring Geothermal Heat Flux from an Ice-Borehole Temperature Profile at Law Dome, East Antarctica, Journal of Glaciology, 66, 509–519, https://doi.org/10.1017/jog.2020.27, 2020.

Morgan, VI., Wookey, CW., Li, J., Van Ommen, TD., Skinner, W., and Fitzpatrick, MF.: Site Information and Initial Results from Deep Ice Drilling on Law Dome, Antarctica, Journal of Glaciology, 43, 3–10, 1997.

460 Morlighem, M., Rignot, E., Seroussi, H., Larour, E., Ben Dhia, H., and Aubry, D.: Spatial Patterns of Basal Drag Inferred Using Control Methods from a Full-Stokes and Simpler Models for Pine Island Glacier, West Antarctica, Geophysical Research Letters, 37, https://doi.org/10.1029/2010GL043853, 2010.

Morlighem, M., Rignot, E., Binder, T., Blankenship, D., Drews, R., Eagles, G., Eisen, O., Ferraccioli, F., Forsberg, R., Fretwell, P., Goel, V., Greenbaum, J. S., Gudmundsson, H., Guo, J., Helm, V., Hofstede, C., Howat, I., Humbert, A., Jokat, W., Karlsson, N. B., Lee, W. S.,
465 Matsuoka, K., Millan, R., Mouginot, J., Paden, J., Pattyn, F., Roberts, J., Rosier, S., Ruppel, A., Seroussi, H., Smith, E. C., Steinhage, D., Sun, B., van den Broeke, M. R., van Ommen, T. D., van Wessem, M., and Young, D. A.: Deep Glacial Troughs and Stabilizing Ridges Unveiled beneath the Margins of the Antarctic Ice Sheet, Nature Geoscience, 13, 132–137, https://doi.org/10.1038/s41561-019-0510-8, 2020.

Motoyama, H.: The Second Deep Ice Coring Project at Dome Fuji, Antarctica, Scientific Drilling, 5, 41–43, https://doi.org/10.5194/sd-5-41-
470 2007, 2007.

Mouginot, J., Scheuchl, B., and Rignot, E.: Mapping of Ice Motion in Antarctica Using Synthetic-Aperture Radar Data, Remote Sensing, 4, 2753–2767, 2012.

Mulvaney, R., Rix, J., Polfrey, S., Grieman, M., Martìn, C., Nehrbass-Ahles, C., Rowell, I., Tuckwell, R., and Wolff, E.: Ice Drilling on Skytrain Ice Rise and Sherman Island, Antarctica, Annals of Glaciology, 62, 311–323, https://doi.org/10.1017/aog.2021.7, 2021.

475   Nagornov, OV., Konovalov, Y. V., Zagorodnov, VS., and Thompson, LG.: Reconstruction of the Surface Temperature of Arctic Glaciers from the Data of Temperature Measurements in Wells, Journal of engineering physics and thermophysics, 74, 253–265, 2001.

Parrenin, F., Dreyfus, G., Durand, G., Fujita, S., Gagliardini, O., Gillet, F., Jouzel, J., Kawamura, K., Lhomme, N., Masson-Delmotte, V., Ritz, C., Schwander, J., Shoji, H., Uemura, R., Watanabe, O., and Yoshida, N.: 1-D-ice Flow Modelling at EPICA Dome C and Dome Fuji, East Antarctica, Climate of the Past, 3, 243–259, https://doi.org/10.5194/cp-3-243-2007, 2007.

480   Pattyn, F.: A New Three-dimensional Higher-order Thermomechanical Ice Sheet Model: Basic Sensitivity, Ice Stream Development, and Ice Flow across Subglacial Lakes, Journal of Geophysical Research: Solid Earth, 108, 2003.

Pattyn, F.: Antarctic Subglacial Conditions Inferred from a Hybrid Ice Sheet/Ice Stream Model, Earth and Planetary Science Letters, 295, 451–461, https://doi.org/10.1016/j.epsl.2010.04.025, 2010.

Pattyn, F., Perichon, L., Aschwanden, A., Breuer, B., de Smedt, B., Gagliardini, O., Gudmundsson, G. H., Hindmarsh, R. C. A., Hubbard, A.,
485   Johnson, J. V., Kleiner, T., Konovalov, Y., Martin, C., Payne, A. J., Pollard, D., and Price, S.: Benchmark Experiments for Higher-Order and Full-Stokes Ice Sheet Models (ISMIP–HOM), The Cryosphere, p. 14, 2008.

Pettit, E. C., Waddington, E. D., Harrison, W. D., Thorsteinsson, T., Elsberg, D., Morack, J., and Zumberge, M. A.: The Crossover Stress, Anisotropy and the Ice Flow Law at Siple Dome, West Antarctica, Journal of Glaciology, 57, 39–52, https://doi.org/10.3189/002214311795306619, 2011.

490   Pollard, D. and DeConto, R. M.: Description of a Hybrid Ice Sheet-Shelf Model, and Application to Antarctica, Geoscientific Model Development, 5, 1273–1295, https://doi.org/10.5194/gmd-5-1273-2012, 2012.

Priscu, J. C., Kalin, J., Winans, J., Campbell, T., Siegfried, M. R., Skidmore, M., Dore, J. E., Leventer, A., Harwood, D. M., Duling, D., Zook, R., Burnett, J., Gibson, D., Krula, E., Mironov, A., McManis, J., Roberts, G., Rosenheim, B. E., Christner, B. C., Kasic, K., Fricker, H. A., Lyons, W. B., Barker, J., Bowling, M., Collins, B., Davis, C., Gagnon, A., Gardner, C., Gustafson, C., Kim, O.-S., Li,
495   W., Michaud, A., Patterson, M. O., Tranter, M., Venturelli, R., Vick-Majors, T., Elsworth, C., and The SALSA Science Team: Scientific Access into Mercer Subglacial Lake: Scientific Objectives, Drilling Operations and Initial Observations, Annals of Glaciology, 62, 340–352, https://doi.org/10.1017/aog.2021.10, 2021.

Rückamp, M., Humbert, A., Kleiner, T., Morlighem, M., and Seroussi, H.: Extended Enthalpy Formulations in the Ice-sheet and Sea-level System Model (ISSM) Version 4.17: Discontinuous Conductivity and Anisotropic Streamline Upwind Petrov–Galerkin (SUPG) Method,
500   Geoscientific Model Development, 13, 4491–4501, https://doi.org/10.5194/gmd-13-4491-2020, 2020.

Scambos, T. A.: Glacier Acceleration and Thinning after Ice Shelf Collapse in the Larsen B Embayment, Antarctica, Geophysical Research Letters, 31, L18 402, https://doi.org/10.1029/2004GL020670, 2004.

Schlegel, N.-J., Seroussi, H., Schodlok, M. P., Larour, E. Y., Boening, C., Limonadi, D., Watkins, M. M., Morlighem, M., and van den Broeke, M. R.: Exploration of Antarctic Ice Sheet 100-Year Contribution to Sea Level Rise and Associated Model Uncertainties Using
505   the ISSM Framework, The Cryosphere, 12, 3511–3534, https://doi.org/10.5194/tc-12-3511-2018, 2018.

Schlegel, NJ., Larour, E., Seroussi, H., Morlighem, M., and Box, JE.: Decadal-scale Sensitivity of Northeast Greenland Ice Flow to Errors in Surface Mass Balance Using ISSM, Journal of Geophysical Research: Earth Surface, 118, 667–680, 2013.

Schoof, C.: Marine Ice-Sheet Dynamics. Part 1. The Case of Rapid Sliding, Journal of Fluid Mechanics, 573, 27–55, https://doi.org/10.1017/S0022112006003570, 2007.

510   Seroussi, H., Morlighem, M., Rignot, E., Khazendar, A., Larour, E., and Mouginot, J.: Dependence of Century-Scale Projections of the Greenland Ice Sheet on Its Thermal Regime, Journal of Glaciology, 59, 1024–1034, https://doi.org/10.3189/2013JoG13J054, 2013.

Seroussi, H., Ivins, E. R., Wiens, D. A., and Bondzio, J.: Influence of a West Antarctic Mantle Plume on Ice Sheet Basal Conditions, Journal of Geophysical Research: Solid Earth, 122, 7127–7155, https://doi.org/10.1002/2017JB014423, 2017.

Seroussi, H., Nowicki, S., Payne, A. J., Goelzer, H., Lipscomb, W. H., Abe-Ouchi, A., Agosta, C., Albrecht, T., Asay-Davis, X., and Barthel,
515   A.: ISMIP6 Antarctica: A Multi-Model Ensemble of the Antarctic Ice Sheet Evolution over the 21st Century, The Cryosphere, 14, 3033–3070, 2020.

Shapiro, N. M. and Ritzwoller, M. H.: Inferring Surface Heat Flux Distributions Guided by a Global Seismic Model: Particular Application to Antarctica, Earth and Planetary Science Letters, 223, 213–224, 2004.

Slawny, K. R., Johnson, J. A., Mortensen, N. B., Gibson, C. J., Goetz, J. J., Shturmakov, A. J., Lebar, D. A., and Wendricks, A. W.: Production
520   Drilling at WAIS Divide, Annals of Glaciology, 55, 147–155, https://doi.org/10.3189/2014AoG68A018, 2014.

Smith, A. M., Anker, P. G. D., Nicholls, K. W., Makinson, K., Murray, T., Rios-Costas, S., Brisbourne, A. M., Hodgson, D. A., Schlegel, R.,
and Anandakrishnan, S.: Ice Stream Subglacial Access for Ice-Sheet History and Fast Ice Flow: The BEAMISH Project on Rutford Ice
Stream, West Antarctica and Initial Results on Basal Conditions, Annals of Glaciology, 62, 203–211, https://doi.org/10.1017/aog.2020.82,
2021.

525   Smith, B. E., Gourmelen, N., Huth, A., and Joughin, I.: Connected Subglacial Lake Drainage beneath Thwaites Glacier, West Antarctica,
The Cryosphere, 11, 451–467, https://doi.org/10.5194/tc-11-451-2017, 2017.

Smith-Johnsen, S., de Fleurian, B., Schlegel, N., Seroussi, H., and Nisancioglu, K.: Exceptionally High Heat Flux Needed to Sustain the
Northeast Greenland Ice Stream, The Cryosphere, 14, 841–854, https://doi.org/10.5194/tc-14-841-2020, 2020a.

Smith-Johnsen, S., Schlegel, N.-J., de Fleurian, B., and Nisancioglu, K. H.: Sensitivity of the Northeast Greenland Ice Stream to Geothermal
530   Heat, Journal of Geophysical Research: Earth Surface, 125, e2019JF005 252, 2020b.

Talalay, P., Li, Y., Augustin, L., Clow, G. D., Hong, J., Lefebvre, E., Markov, A., Motoyama, H., and Ritz, C.: Geothermal Heat Flux from
Measured Temperature Profiles in Deep Ice Boreholes in Antarctica, The Cryosphere, 14, 4021–4037, https://doi.org/10.5194/tc-14-4021-2020, 2020.

Van Ommen, TD., Morgan, VI., Jacka, TH., Woon, S., and Elcheikh, A.: Near-Surface Temperatures in the Dome Summit South (Law Dome,
535   East Antarctica) Borehole, Annals of Glaciology, 29, 141–144, 1999.

WAIS Divide Project Members: Onset of Deglacial Warming in West Antarctica Driven by Local Orbital Forcing, Nature, 500, 440–444,
https://doi.org/10.1038/nature12376, 2013.

Yang, J.-W., Han, Y., Orsi, A. J., Kim, S.-J., Han, H., Ryu, Y., Jang, Y., Moon, J., Choi, T., Hur, S. D., and Ahn, J.: Surface Temperature in
Twentieth Century at the Styx Glacier, Northern Victoria Land, Antarctica, From Borehole Thermometry, Geophysical Research Letters,
540   45, 9834–9842, https://doi.org/10.1029/2018GL078770, 2018.

Zagorodnov, V., Nagornov, O., Scambos, TA., Muto, A., Mosley-Thompson, E., Pettit, EC., and Tyuflin, S.: Borehole Temperatures Reveal
Details of 20th Century Warming at Bruce Plateau, Antarctic Peninsula, The Cryosphere, 6, 675–686, 2012.